minerals

MDPI

Article

Microstructural Insights into the Evolution of Ophiolitic Chromite from Luobusha

Yu Yang [1,2,*], Jingsui Yang [1], Weiwei Wu [3,*], Pengjie Cai [1] and Haitao Ma [1]

[1] State Key Laboratory for Mineral Deposits Research, School of Earth Sciences and Engineering, Nanjing University, Nanjing 210093, China
[2] SinoProbe Lab., Chinese Academy of Geological Sciences (CAGS), Beijing 100037, China
[3] Institute of Geology and Geophysics, Chinese Academy of Sciences, Beijing 100029, China
* Correspondence: yangyugeo@nju.edu.cn (Y.Y.); cugcags@163.com (W.W.)

Abstract: The podiform chromitite found within the Luobusha ophiolite comprises characteristic nodules and massive chromitites. However, the exact origin of these formations remains a topic of ongoing debate. In this study, the microstructures of olivine and chromite are investigated to unravel their formation processes and shed light on the associated geodynamic mechanisms. EBSD analysis provides insights into chromitite and host peridotite deformation mechanisms. Olivine grains in the host dunite and nodular chromite exhibit crystallographic preferred orientations (CPOs) with D-type fabrics, which show a girdle distribution in the [010] and [001] axes, normal to the foliation plane of the sample. The massive and disseminated chromitite displays B-type and C-type olivine fabric, with a concentration of [001] axes parallel to the lineation of the sample. Crystal plastic deformation can be observed in the Luobusha chromite grains, highlighting intercrystalline deformation processes. Small grains lacking misorientation observed in the massive chromitite are likely attributed to heterogeneous nucleation. Chromite nodules are found to be a patchwork of subgrains with various orientations and high-angle boundary misorientation. The formation of Luobusha chromitite involves deep-seated crystallization, followed by amalgamation, and subsequent deformation within the mantle peridotite. These findings distinguish Luobusha chromitite from other ophiolitic chromite deposits, offering valuable insights into the deformation history and formation processes.

Keywords: ophiolitic chromite; electron backscatter diffraction; misorientation; microstructural evolution; crystallographic preferred orientation

Citation: Yang, Y.; Yang, J.; Wu, W.; Cai, P.; Ma, H. Microstructural Insights into the Evolution of Ophiolitic Chromite from Luobusha. *Minerals* **2023**, *13*, 1047. https://doi.org/10.3390/min13081047

Academic Editor: Shoji Arai

Received: 6 June 2023
Revised: 30 July 2023
Accepted: 30 July 2023
Published: 7 August 2023

1. Introduction

Podiform-type chromitites, one of the typical chromite deposits, are commonly hosted in ophiolites and modern oceanic peridotites, underlying the uppermost part of mantle [1]. The term "podiform" refers to the distinct dunite envelope surrounding the chromitite pods, which exhibit varying patterns of chromite grains, including schlieren, orbicular, nodular, and anti-nodular textures [2–4]. In addition to the classical pod-like microstructure, other textures, such as massive disseminated layers, have also been observed in ophiolitic podiform chromitites. Ophiolites, considered remnants of ancient oceanic lithosphere, provide valuable insights into the recycling of materials within the lithosphere and are significant for plate tectonic models related to the recycling of oceanic crust [5,6]. Thus, as a unique part of ophiolites, the genesis of ophiolitic podiform chromitites and the associated peridotites is a fundamental aspect of plate tectonic models that are related to the recycling of the oceanic crust. Yet, after the decades-long debate, they remain unclear.

One proposed mechanism suggests that chromitites form through interactions between melts and peridotite, followed by the mixing of tholeiitic or boninitic magmas at shallow depths [7,8]. However, the discovery of high-pressure phases, such as diamonds and coesite, as well as super-reducing phases, like Ni-Mn-Co alloys and nitrides, within podiform chromitites challenges the low-pressure formation hypothesis [9,10]. These observations,

coupled with unusual microfabrics, like clinopyroxene exsolution lamellae in chromite, suggest that the formation pressures may exceed 14 GPa, equivalent to the top of the mantle transition zone [10]. Due to its high hardness and high melting point, chromite is relatively resistant to deformation and metamorphic alteration compared to the host rocks. Therefore, podiform chromitites offer valuable insights into understanding the metallogeny of ophiolitic chrome ores and the deep crustal recycling model, providing a pristine record for investigation.

Microstructural information and crystallographic preferred orientations (CPOs) deliver significant perspectives on plastic deformation mechanisms and rheology. The deformation of crystals in chromitites and hosting rocks is primarily governed by dislocation creep, potentially accompanied by nucleation, subgrain rotation, and grain boundary sliding. The characteristics of the CPOs, such as symmetry and intensity, are known to be influenced by the deformation processes imposed on the rocks. These processes are affected by various factors, including temperature, deviatoric stress, strain rate, rheologic regime, and the presence of fluids/melts. They might leave distinct signatures on the microstructures and either enhance or weaken the CPOs. The dominant deformation mechanism is reflected in the final CPOs [11]. Therefore, the evolution of mineral CPOs, such as olivine, pyroxene, and chromite, plays a crucial role in understanding the deformation processes within the ophiolitic mantle. In this study, we investigate the microstructural features, including CPOs, misorientations, grain size, and shape factor, of podiform chromitites from Luobusha, located in the eastern segment of the Neo-Tethyan suture.

2. Materials and Methods

2.1. Geological Setting

The Luobusha ophiolite originated from mid-ocean ridge processes and, subsequently, underwent boninitic magmatism in a suprasubduction zone (SSZ) setting [12,13]. It serves as a key indicator of the evolution of the Tethyan Ocean during the Early to Middle Jurassic, as well as the subduction events that occurred in the Early Cretaceous [14,15]. The ophiolite is oriented approximately in an east–west direction, spanning a length of around 37 km and a width of approximately 3 km, covering an area of 70 km^2. It is characterized by overthrusting onto Tertiary conglomerate and sandstone toward the north, as well as thrusting by the Upper Triassic flysch sequence toward the south, separated by south-dipping faults (Figure 1) [16]. The Luobusha ophiolite comprises mantle peridotite, cumulate, and mafic rocks, with the mantle sequence dominated by harzburgite, dunite, and a small amount of lherzolite.

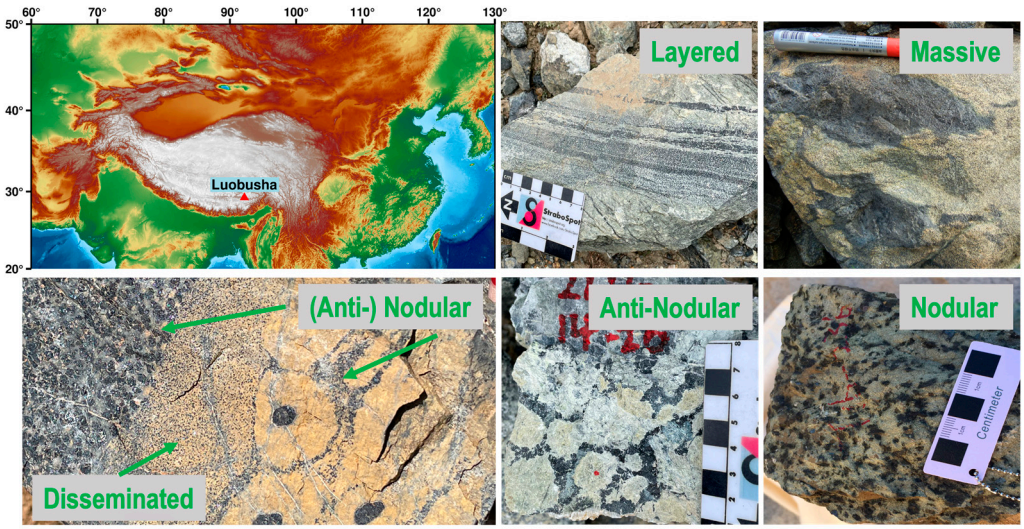

Figure 1. Field photographs showing Luobusha podiform chromites.

The podiform chromitites within the Luobusha ophiolite are enclosed by dunite and are predominantly found in harzburgite rocks [17,18]. The chromitites display a variety of ore textures, including disseminated, layered, (anti-) nodular, and massive structures (Figure 1). The chromite grains in nodules are euhedral to subhedral in shape, whereas the olivine grains surrounding nodules retain only a few fresh and euhedral shapes, with the majority exhibiting irregular outlines due to serpentinization. Approximately, 5 million tons of chromite ore is estimated to be present in the entirety of the Luobusha ophiolite [19]. In this study, dunite was chosen as the host rock, and the three categories of chromitite studied were nodular, disseminated, and massive.

2.2. Crystal Orientation and Texture Measurements

Mineral fabrics were analyzed using scanning electron microscopy coupled with electron backscatter diffraction (SEM-EBSD) at the Institute of Geology, China Earthquake Administration, China, using a Zeiss Sigma scanning electron microscope (SEM) equipped with an Oxford Nordlys Nano EBSD system. The focus of the analysis was on the microstructures and textures of the primary minerals, specifically olivine and chromite, to gain insights into their deformation history and tectonic processes, serving as indicators for the Luobusha ophiolite in the Neo-Tethyan Ocean. Crystal orientation images were obtained using Oxford Instruments AZtecHKL Acquisition Software, with a step size of 11 µm and a working distance of 25 mm. Automatic indexing was performed during pattern acquisition using AZtec software. The acquired data were processed using CHANNEL 5 software to reduce noise and fill in missing data, ensuring at least 8 neighboring points with similar orientations. The resulting EBSD data is presented in Figure 2.

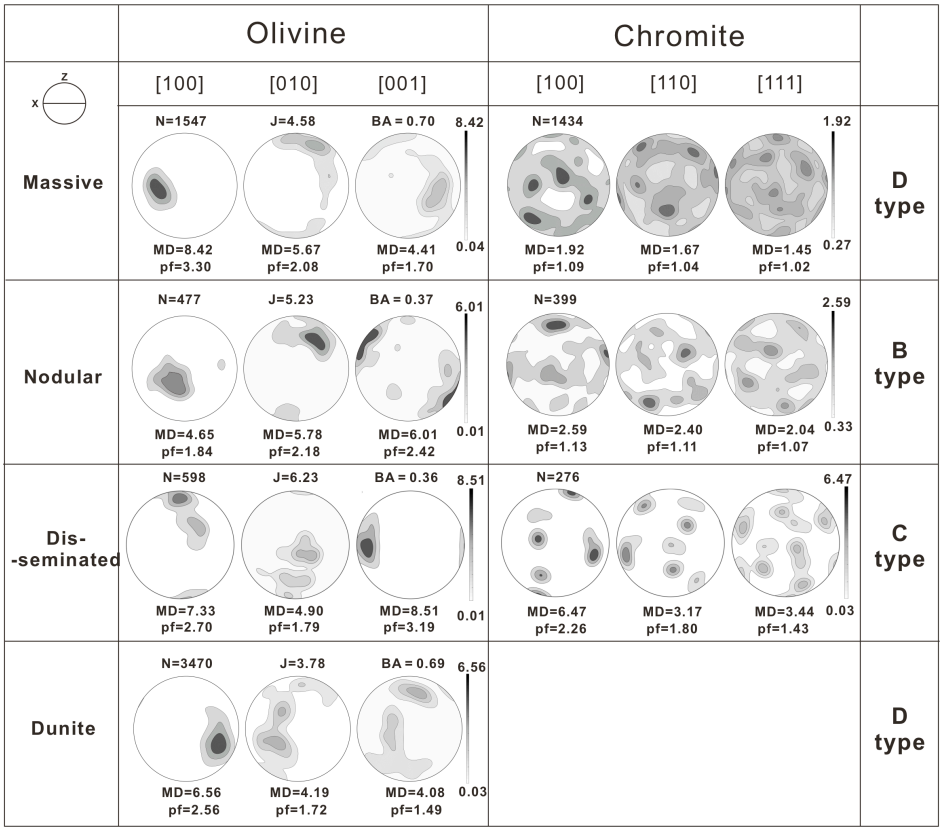

Figure 2. Representative olivine CPO data from Luobusha are presented in equal-area, upper-hemisphere projections. Contours are multiples of uniform distribution. The structural reference frame is shown as insert, where the foliation is horizontal and lineation is E–W. N is the number of grains, MD is the maximum density and pf is an index of fabric intensity. J-index and BA-index stand for the fabric strength and symmetry of orientation distribution.

The J-index is a reliable metric for assessing the strength of CPOs. It is calculated from the volume-averaged integral of the squared orientation densities and is sensitive to any spikes in the orientation distribution function [20]. A J-index of 1 indicates a random distribution, while a J-index of infinity corresponds to a single crystal or a perfect CPO. The BA-index provides information about the axial symmetry in the arrangement of orientations [21]. It is derived from the eigenvalues of the orientation tensors associated with certain crystallographic directions. In the case of analyzing the symmetry of olivine texture, a BA-index can be defined as follows:

$$\text{BA-index} = 1/2\left(2 - \left(\frac{P010}{G010 - P010}\right) - \left(\frac{G100}{G100 + P100}\right)\right) \quad (1)$$

Here, *P*010 represents the point maximum and G010 represents the girdle of the [010] directions. The BA-ndex helps classify the symmetry of olivine CPO into three categories: axial-[010], which is marked by a concentrated point of [010] and a dispersed distribution of [100] (BA-index < 0.35); orthorhombic, characterized by concentrated points of both [100] and [010] (0.35 < BA-index < 0.65); and axial-[100], which is marked by a concentrated point of [100] and a dispersed distribution of [010] (BA-index > 0.65).

3. Results

The CPOs data (Figure 2) are presented in pole figures, which are equal-area, upper-hemisphere projections. To ensure a balanced representation, each pixel in the figures corresponds to one grain, preventing undue emphasis on larger crystals. This approach allows for a focused analysis at the individual grain level rather than coarse-grained aggregates. For ease of comparison, we rotated the CPOs data of all samples to a standardized orientation. Since the foliation and lineation of the samples could not be determined, the data were aligned to a common reference frame. In this reference orientation, the highest concentration of olivine main axes aligns with the lineation (X-direction), while the second highest concentration is perpendicular to the foliation plane (X-Y plane). This reorientation is justified based on previous analyses of olivine CPO, which indicate that the stronger concentration of axes corresponds to the dominant slip system, while the weaker concentration of the remaining axis is a consequence of the orientation of the other two axes.

3.1. Peridotite CPO Patterns and Fabric Strength

The olivine fabric pattern in the dunite and massive chromitite sample showed D-type CPO [22], which was identified by a concentration of [100] axes close to the lineation, with [010] and [001] axes aligned in a girdle distribution normal to the foliation. The olivine in these samples exhibited a relatively weak CPO (J-index < 5) and a higher axial-[100] tendency with a BA-index of approximately 0.70, compared to the nodular and disseminated chromitite, which had a BA-index of around 0.37. In the nodular chromitite, the olivine fabric pattern is referred to as B-type CPO [22], with the maximum concentration of olivine [001] occurring in the X-direction and [010] directions concentrated parallel to the Z-directions. The C-type CPO pattern [23], as characterized by a clustering of [001] axes near the lineation and [100] axes concentrated perpendicular to the foliation, was observed in the olivine of disseminated chromitite. The J-index of olivine in the nodular and disseminated chromitite ranged from 5.23 to 6.23, which is less than those analyzed in similar ophiolitic rock, such as the Oman ophiolite and Mayoumu ophiolite in the western Yarlung Zangbo Suture zone [24,25]. The pf-index was employed to determine the fabric strength of the principal crystallographic axes in each sample [26,27]. This index has a value of 1 for randomly oriented crystals and an infinite value for a single crystal. For most natural peridotites, the pf-index values range from 2 to 20 [20]. The olivine crystallographic axes strengths observed in the Luobusha samples were similar to pf-index values ranging from 1.49 to 3.30 (Figure 2).

The M2M index was employed to quantify the intracrystalline orientation gradients through the analysis of the misorientation of individual pixels relative to the mean ori-

entation of the grain [28]. The olivine in the chromitite displayed a significantly lower M2M value ($\leq 3^{\circ}$) compared to the olivine in the dunite (7.03°) (Table 1). The shape factor, defined as the ratio of a grain's perimeter to that of a circle with the equivalent area, is used to assess the sinuosity of grain boundaries. The olivine in the massive and nodular chromitite had similar shape factor values (~1.67), which are relatively lower than those of the olivine in the disseminated chromitite and dunite (~4.50) (Table 1). The recrystallized area fractions for olivine were evaluated as the proportion of the area occupied by grains with a spread in orientation (GOS) of less than 1.5° relative to the total area occupied by olivine grains. The dunite showed minimal recrystallization (5%), whereas the chromitite exhibited some degree of recrystallization, particularly in the nodular chromitite (65%) (Table 1). Significant differences in olivine grain size were observed between the dunite and chromitite, with larger grain sizes observed in the dunite (9.2×10^4) compared to the chromitite (1.9×10^4). Among the three types of chromitites, the olivine in the massive chromitite had the largest grain size (Table 1).

Table 1. Quantitative microstructures, CPO parameters derived from EBSD mapping for olivine and chromite in Luobusha chromitite ore deposit.

Rock Type	Modal Proportions (%)			CPO Parameters for Olivine					Shape Factor		Grain Area (μm^2)	
	Ol	Chr	Py	J-index	BA-index	M2M	Rex	Fabric	Ol	Chr	Ol	Chr
Nodular Chromitite	12	87	1	5.23	0.37	1.45	65%	B-type	1.66	2.40	1.6×10^4	27.7×10^4
Disseminated Chromitite	61	21	18	6.23	0.36	1.32	26%	C-type	4.43	3.70	1.9×10^4	0.6×10^4
Massive Chromitite	40	59	1	4.58	0.70	2.97	11%	D-type	1.67	7.87	5.5×10^4	9.2×10^4
Dunite	96	1	3	3.78	0.69	7.03	5%	D-type	4.60	-	9.2×10^4	-

The reported values are weighted averages across the entire EBSD map, taking into account the size of each grain. M2M refers to the misorientation of each pixel relative to the grain's average orientation, while Rex represents the fraction of the sample that has undergone recrystallization. The grain area and shape factors are apparent 2D values.

3.2. Orientation Analysis of Chromite

EBSD analysis also revealed that the chromite grains had a weak CPO pattern, characterized by multiple orientation maxima at [100], [110], and [111] (Figure 2). To evaluate the strength of the crystallographic axes, we utilized the pf-index to analyze the CPOs. Our observations indicate that the massive chromitite samples displayed a relatively weak CPO, with pf-index values of 1.09, 1.04, and 1.02 for [100], [110], and [111], respectively. This is slightly different from the coarse grains in nodular chromitite (pf-index values of 1.13, 1.11, and 1.07 for [100], [110], and [111], respectively). However, it is important to note that the small difference in pf-index strength among the samples may be attributed to the number of analyzed points, with only 276 grains being measured in the disseminated chromitite, which showed the strongest strength (pf-index values of 2.26, 1.80, and 1.43 for [100], [110], and [111], respectively).

Our findings suggest that the chromite grains analyzed in this study have a relatively high average internal misorientation per grain (M2M), as compared to similar grains from Turkey and Bushveld, with misorientation angles ranging from 1.76° to 3.98° [29,30]. Among the chromite grains, those from the nodular chromitite exhibited the highest M2M values, with misorientation angles showing a gradual increase from the core to the rim, occasionally accompanied by sudden jumps (Figure 3). These misorientations were mostly located at the rim of the grains, which may be indicative of deformation and "welding" between adjacent grains following a collision event (Figure 3). Moreover, the average orientation of the nodules indicates that they comprised a variety of chromite grains, each

having unique orientations in relation to the other grains. There seemed to be no discernible orientation relationship among the chromite grains within the same nodule (Figure 3).

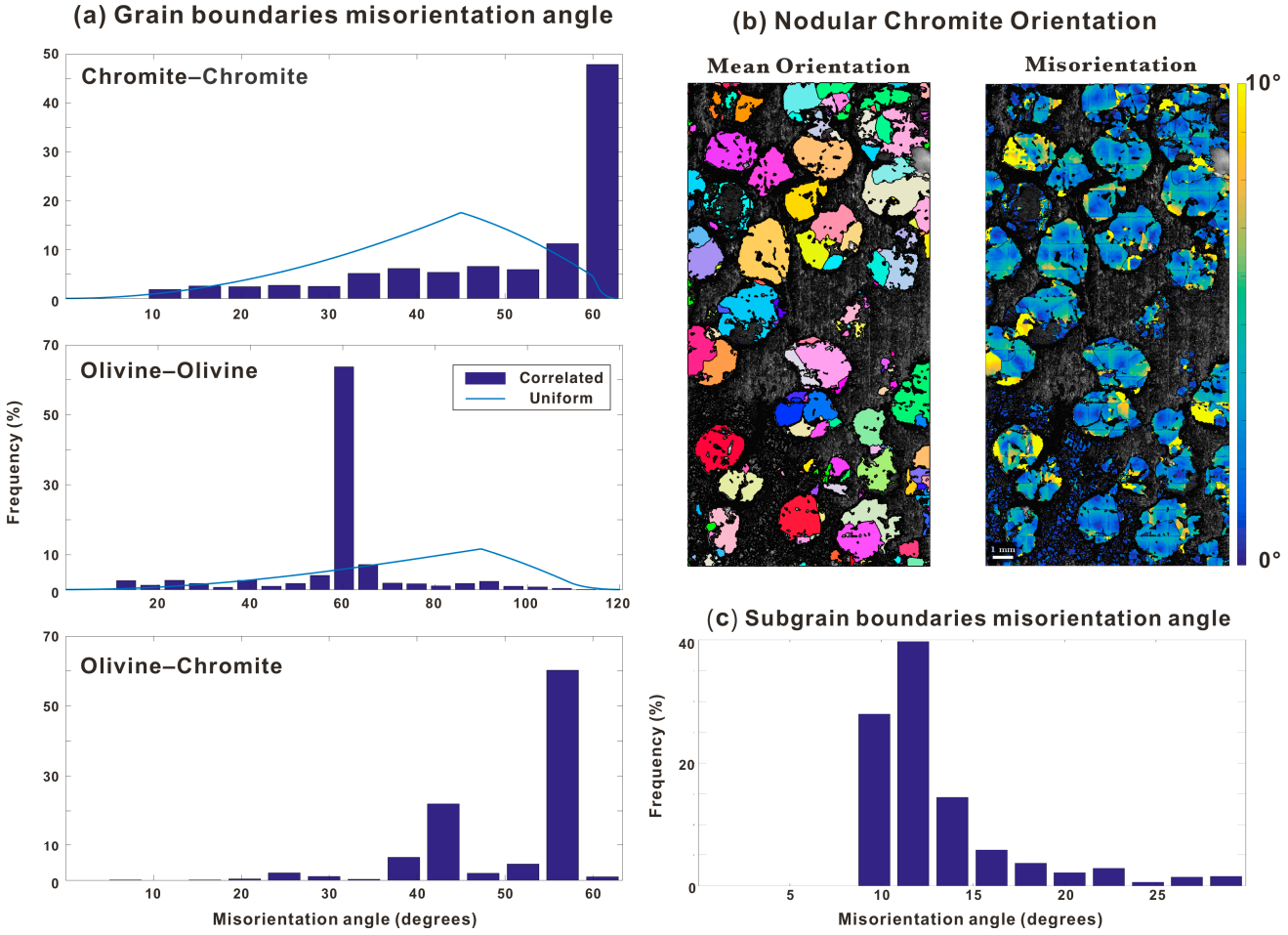

Figure 3. The nodular chromitite microstructure: (**a**) grain boundaries misorientation angle distribution. The light blue line is calculated for a statistically random distribution. (**b**) Nodular chromite orientation including the mean orientation and misorientation. The coloring of the mean orientation is done using Euler angle color coding. (**c**) Chromite subgrain boundaries misorientation angle distribution.

3.3. Grain Boundary Analysis

Subgrain boundaries and continuous crystal bending were common in both the nodular and massive chromitite, resulting in crystal–plastic deformation (Figures 3 and 4). In the nodular and massive chromitite, subgrain boundaries commonly occurred with high angles (> 5° orientation change across the boundary). The misorientation distribution of the subgrain showed a wider range (8°–28°), compared to that of the massive chromitite, which ranged from 10° to 19°. The most prevalent range of misorientation in chromite subgrain boundaries fell between 10° and 14°, accounting for approximately 70% of the samples (Figures 3 and 4). Due to the small grain size and the limited number of grains in the disseminated chromitite, the microstructure and intracrystalline properties observed may not be representative for discussion.

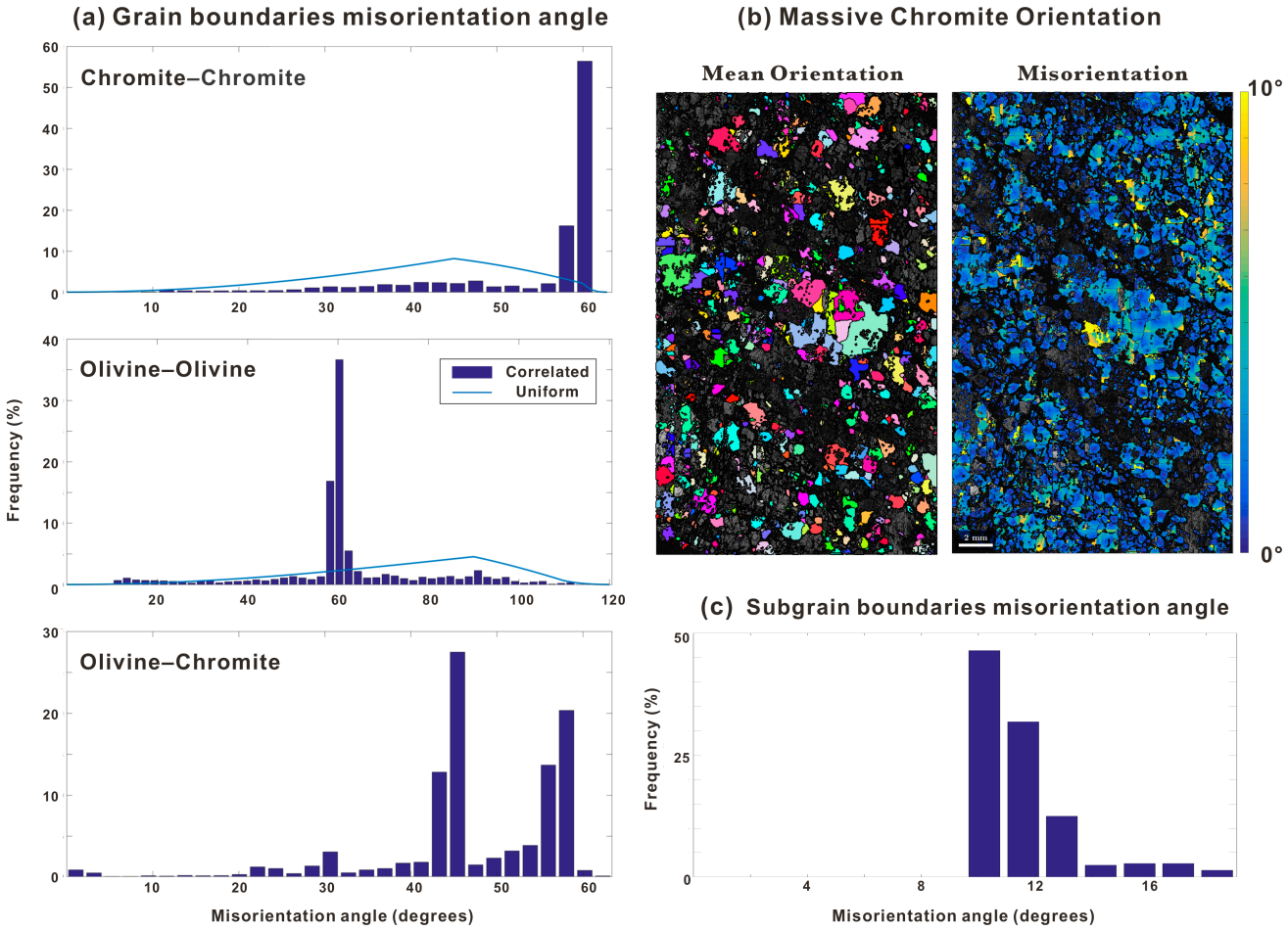

Figure 4. The massive chromitite microstructure: (**a**) grain boundaries misorientation angle distribution. The light blue line is calculated for a statistically random distribution. (**b**) Massive chromitite orientation including the mean orientation and misorientation. The coloring of the mean orientation is done using Euler angle color coding. (**c**) Chromite subgrain boundaries misorientation angle distribution.

In addition, we calculated the misorientation from the neighboring grain orientations on either side of a boundary to search for a special relationship along olivine–olivine boundaries, olivine–chromite boundaries, and chromite–chromite boundaries. In terms of the results, the orientation of the grain boundaries in the chromite of Luobusha exhibited a correlation, which differs significantly from the random characteristics of the chromite in Oman [31]. In the nodular and massive chromitite, the distribution of the misorientation angle along the chromite–chromite boundary predominantly occurred at 60°, accounting for over 50% of the observations. Similarly, the boundaries between olivine and chromite exhibited a noticeable distribution, with the peak occurring at 45° in massive chromitite and 55° in nodular chromitite (Figures 3 and 4).

4. Discussion

The Luobusha chromitites demonstrate distinctive microstructures, displaying unique features within different domains. The variations observed in microstructural patterns, specifically associated with the different fabric types of the host olivine, may be attributed to the deformation conditions and their respective histories.

4.1. Deformation Processes Constraints from Olivine Grains

The nodular chromitite exhibited a B-type olivine CPO, while the disseminated chromitite displayed a C-type CPO. This observation is in good agreement with the work of Yu [32] on the peridotites from the same locality, which suggests that B- and C-type fabrics form at significant depths (>200 km), with temperatures ranging from 950 to 1080 °C. In contrast, the microstructures of the dunite and massive chromitite revealed a D-type olivine CPO pattern. The D-type olivine pattern has been documented in lithospheric shear zones [20,33], natural peridotite from fore-arc and back-arc settings [24,34], and ophiolite settings [35,36]. A D-type fabric is often associated with [100]-slip systems, where a slip primarily occurs on the [100]{0kl} family [23]. The dominance of [100]-slip olivine in the plastic deformation, as opposed to [001]-slip (e.g., B- and C-type fabric), implies higher temperatures potentially exceeding 1150 °C [37–39]. Furthermore, experimental studies on the activity of olivine slip systems have indicated that D-type fabric is commonly observed under high-stress and dry conditions [37,40,41].

The average M2M value, calculated across the entire sample, was employed as an indicator to quantify the level of recrystallization [28]. The recovery and growth of grains with lower dislocation densities, such as newly crystallized or recrystallized grains, contribute to a reduction in the mean M2M value. In the dunite and massive chromitite, olivine exhibiting [100]-slip patterns (D-type) showed a relatively lower degree of recrystallization, as indicated by the higher M2M value, compared to the predominance of the [001]-slip olivine pattern (B- and C-type) in the disseminated and nodular chromitite (Table 1). This variation in CPO patterns might suggest a dependency on the extent of recrystallization and the associated "preferred" slip system. Grains oriented in challenging configurations, such as those with [100] parallel to stress σ1, experience pronounced kinking and serve as preferential sites for recrystallization [11,27]., The [100]-slip CPO varies due to weak fabric intensities during dynamic recrystallization and grain size reduction [27]. These observations imply selective recrystallization occurs in grains with D-type fabric, leading to the development of other CPOs associated with "easy" slip systems [27].

4.2. Formation of Luobusha Chromitite

The Luobusha chromite grains are characterized by crystal plastic deformation, displaying distinct intercrystalline deformation including continuous crystal bending and subgrain boundaries. Grain boundaries exhibit specific crystallographic relationships, suggesting that they are non-random and non-open boundaries that restrict the flow of melts or fluids [31,42]. In the massive chromitite, the presence of D-type olivine fabric suggests the occurrence of high-stress plastic deformation. In such cases, a reduction in grain size is typically accommodated through strain, as evidenced by the smaller grain sizes of chromite compared to nodular chromitite (Table 1). Three primary mechanisms contribute to grain size reduction: (1) bulging (BLG) recrystallization facilitated by grain boundary migration, (2) subgrain rotation recrystallization (SGR), and (3) heterogeneous nucleation and growth of new grains [43–45]. At low temperatures, localized BLG recrystallization occurs, characterized by the presence of old grain remnants surrounded by moats of recrystallized grains, forming a core-and-mantle structure [45]. However, it is evidently not applicable in our case. SGR, on the other hand, involves the recrystallization of subgrains through rotational processes, where the continuous accumulation of dislocations along subgrain boundaries transforms their low-angle boundaries into high-angle boundaries [44]. Theoretically, subgrain rotation increases the frequency of intermediate angle boundaries (5°–15°) while reducing the occurrence of low-angle boundaries (<5°) [46], leading to internal deformation features akin to those of the host grains [47]. This aligns with the high frequency of intermediate-angle chromite subgrain boundaries observed in the massive chromitite of Luobusha

In regions experiencing high levels of strain within the grains, the occurrence of heterogeneous nucleation and growth of new grains is expected, as this contributes to a reduction in strain and dislocation density. The migration of grain boundaries, which is

triggered by strain, facilitates the formation of new strain-free grains. In the presence of intense deformation, if the nucleus or newly formed grain continues to grow, it encounters a continuous succession of new crystallographic orientations and additional deformation microstructures, such as dense dislocation walls and subgrains. The observation of small grains in the massive chromitite, which lack significant misorientation but exhibit different mean orientations, suggests that the processes of heterogeneous nucleation and grain growth remain latent within the deformed state. However, these processes do not give rise to the formation of additional deformation microstructures, such as subgrains (Figure 4).

A detailed EBSD analysis of chromite nodules revealed a wide range of crystallographic orientations within the nodules, indicating that they are predominantly composed of randomly oriented chromite grains. Most nodules primarily consist of amalgamated crystals without a distinct core structure (Figure 3). The formation mechanism of ophiolitic nodular chromitite has been interpreted as a process involving nucleation and growth through skeletal crystals [31,48]. According to this hypothesis, it is anticipated that a rim of small chromite grains would be observed, having precipitated around the skeletal core and subsequently becoming embedded in magma, thereby resulting in the smooth surface of the nodules. The rim grains surrounding the skeletal crystal within the nodules share a common [110] crystallographic axis. In contrast, the chromite grains within the Luobusha nodules are interconnected at different angles (Figure 3). Each nodule contains multiple individual chromite grains, a majority of which present significant lattice distortion (>10° misorientation). This observation implies that the deformation record within the grains predates the assembly of the nodules and potentially captures the history subsequent to crystallization. Following the formation of the nodules, minor deformation also occurred, primarily at the points of contact with neighboring grains.

The misorientation of subgrain boundaries in nodule chromite primarily ranges from 10° to 14°, with approximately 20% of subgrains exhibiting relatively high angles (≥15°). The movement and interaction of dislocations contribute to the formation of subgrain walls, reducing the internal strain energy of the crystals and promoting recovery. The progressive deformation of nodule chromite leads to an increased influx of dislocations into the subgrain walls, resulting in the development of high-angle subgrain boundaries [43–45]. Conversely, massive chromite predominantly exhibits subgrain boundary misorientations lower than 15°, indicating that deformation is accommodated through subgrain rotation or the nucleation of new grains [46,49]. Through olivine fabric analysis, we have determined that nodular chromitite exhibits a higher degree of recrystallization compared to both massive chromitite and the host dunite. This finding implies that nodular chromite grains, in response to deformation and the subsequent release of strain, underwent recrystallization and grain growth. As a result, the interior of these growing grains retains deformation microstructures, documenting the complex history of their formation. In contrast, the internal structure of massive chromite grains appears cleaner, suggesting that, under higher stress conditions, there is limited grain growth. This observation highlights the distinct deformation characteristics between nodular chromitite and massive chromitite, shedding light on the intricate processes of strain release and grain evolution.

5. Conclusions

Based on the analysis of olivine fabric and its strength in Luobusha peridotite and chromitites, it can be inferred that the host dunite or harzburgite underwent deformation in a high-stress, hot, and dry environment prior to the ophiolite outcrop. The olivine fabric manifests three distinct types, which can be roughly categorized into two temperature regimes. In the higher-temperature regime (> 1150 °C), the olivine derived from the dunite and massive chromitite displays a D-type fabric characterized by a low degree of recrystallization. Conversely, in the lower-temperature regime, the olivine within the nodular and disseminated chromitite displays B- and C-type fabric with a high degree of recrystallization. Previous research suggests that the lower-temperature regime corresponds to approximately 1050 °C and a depth of 200 km, indicating that the massive chromitite and

its host dunite in the higher-temperature regime originated from a depth of approximately 250 km.

This study presents evidence suggesting that the formation process of chromite in Luobusha differs from other ophiolitic chromitites, such as those in Oman or Troodos, which have been proposed to crystallize in situ during exposure [31,48]. In contrast, in the Luobusha case, small chromite grains crystallized at greater depths within the mantle and subsequently amalgamated into various structures during deformation with the host mantle peridotite. The massive chromitite in the higher temperature regime, which is hosted by dunite with lower degrees of recrystallization, experienced high-stress deformation involving subgrain rotation and nucleation. On the other hand, the nodular chromite, demonstrating extensive recrystallization of its host, developed through the subgrain coalescence in a lower-temperature regime.

Author Contributions: Conceptualization, Y.Y. and W.W.; supervision, J.Y.; methodology, Y.Y. and P.C.; formal analysis, Y.Y., W.W. and H.M.; investigation, Y.Y. and H.M.; resources, J.Y.; writing—original draft preparation, Y.Y.; writing—review and editing, Y.Y., W.W., P.C., H.M. and J.Y. All authors have read and agreed to the published version of this manuscript.

Funding: This research was funded by the National Natural Science Foundation of China (42102248, 92062215, 41972209, 4217264, and 41802055), the China Postdoctoral Science Foundation (2022M721546), the Foundation of State Key Laboratory of Earthquake Dynamics (LED2022B01), and the Postdoctoral Program of Jiangsu Province (2021Z019).

Data Availability Statement: Not applicable.

Acknowledgments: We express our gratitude to three anonymous reviewers and the editors for their inspiring and meticulous comments.

Conflicts of Interest: The authors declare no conflict of interest.

References

1. Arai, S.; Ahmed, A.H. *Secular Change of Chromite Concentration Processes from the Archean to the Phanerozoic, in Processes and Ore Deposits of Ultramafic-Mafic Magmas through Space and Time*; Elsevier: Amsterdam, The Netherlands, 2018; pp. 139–157.
2. Arai, S.; Miura, M. Formation and modification of chromitites in the mantle. *Lithos* **2016**, *264*, 277–295. [CrossRef]
3. Kusky, T.; Huang, Y.; Wang, L.; Robinson, P.T.; Wirth, R.; Polat, A.; Wei, H. Vestiges of early Earth's deep subduction and CHONSP cycle recorded in Archean ophiolitic podiform chromitites. *Earth-Sci. Rev.* **2022**, *227*, 103968. [CrossRef]
4. Yang, J.; Wu, W.; Lian, D.; Rui, H. Peridotites, chromitites and diamonds in ophiolites. *Nat. Rev. Earth Environ.* **2021**, *2*, 198–212. [CrossRef]
5. Dilek, Y.; Furnes, H. Ophiolite genesis and global tectonics: Geochemical and tectonic fingerprinting of ancient oceanic lithosphere. *Bulletin* **2011**, *123*, 387–411. [CrossRef]
6. Kusky, T.M.; Wang, L.; Dilek, Y.; Robinson, P.; Peng, S.; Huang, X. Application of the modern ophiolite concept with special reference to Precambrian ophiolites. *Sci. China Earth Sci.* **2011**, *54*, 315–341. [CrossRef]
7. Arai, S. Characterization of spinel peridotites by olivine-spinel compositional relationships: Review and interpretation. *Chem. Geol.* **1994**, *113*, 191–204. [CrossRef]
8. González-Jiménez, J.M.; Griffin, W.L.; Gervilla, F.; Proenza, J.A.; O'Reilly, S.Y.; Pearson, N.J. Chromitites in ophiolites: How, where, when, why? Part I. A review and new ideas on the origin and significance of platinum-group minerals. *Lithos* **2014**, *189*, 127–139. [CrossRef]
9. Griffin, W.L.; Afonso, J.C.; Belousova, E.A.; Gain, S.E.; Gong, X.-H.; González-Jiménez, J.M.; Howell, D.; Huang, J.-X.; McGowan, N.; Pearson, N.J.; et al. Mantle Recycling: Transition Zone Metamorphism of Tibetan Ophiolitic Peridotites and its Tectonic Implications. *J. Petrol.* **2016**, *57*, 655–684. [CrossRef]
10. Yang, J.; Robinson, P.T.; Dilek, Y. Diamond-bearing ophiolites and their geological occurrence. *Episodes* **2015**, *38*, 344–364. [CrossRef]
11. Tommasi, A.; Mainprice, D.; Canova, G.; Chastel, Y. Viscoplastic self-consistent and equilibrium-based modeling of olivine lattice preferred orientations: Implications for the upper mantle seismic anisotropy. *J. Geophys. Res. Solid Earth* **2000**, *105*, 7893–7908. [CrossRef]
12. Yang, J.; Zhang, Z.; Li, T.F.; Li, Z.L.; Ren, Y.F.; Xu, X.Z.; Ba, D.Z.; Bai, W.J.; Fang, Q.S.; Chen, S.; et al. Unusual minerals from harzburgite, the host rock of the Luobusa chromite deposit, Tibet. *Acta Petrol. Sin.* **2008**, *24*, 1445–1452.
13. Zhou, M.-F.; Robinson, P.T.; Malpas, J.; Edwards, S.J.; Qi, L. REE and PGE geochemical constraints on the formation of dunites in the Luobusa ophiolite, southern Tibet. *J. Petrol.* **2005**, *46*, 615–639. [CrossRef]

14. Malpas, J.; Zhou, M.-F.; Robinson, P.T.; Reynolds, P.H. Geochemical and geochronological constraints on the origin and emplacement of the Yarlung Zangbo ophiolites, Southern Tibet. *Geol. Soc.* **2003**, *218*, 191–206. [CrossRef]
15. Sun, S.; Ji, S.; Michibayashi, K.; Salisbury, M. Effects of olivine fabric, melt-rock reaction, and hydration on the seismic properties of peridotites: Insight from the Luobusha ophiolite in the Tibetan Plateau. *J. Geophys. Res. Solid Earth* **2016**, *121*, 3300–3323. [CrossRef]
16. Zhou, M.F.; Robinson, P.T.; Malpas, J.; Li, Z. Podiform Chromitites in the Luobusa Ophiolite (Southern Tibet): Implications for Melt-Rock Interaction and Chromite Segregation in the Upper Mantle. *J. Petrol.* **1996**, *37*, 3–21. [CrossRef]
17. Huang, M.X.; Yang, J.-J.; Powell, R.; Mo, X. High-pressure metamorphism of serpentinized chromitite at Luobusha (southern Tibet). *Am. J. Sci.* **2014**, *314*, 400–433. [CrossRef]
18. Yang, J.S.; Robinson, P.T.; Dilek, Y. Diamonds in Ophiolites. *Elements* **2014**, *10*, 127–130. [CrossRef]
19. Zhang, H.; Ba, D.Z.; Guo, T.Y.; Mo, X.X.; Xue, J.Z.; Ruan, G.F.; Wang, Z.Y. *Study of Luobusa Typical Chromite Ore Deposit Qusong County, Tibet (Xizang)*; Xizang People's Publishing House: Lhasa, China, 1996; pp. 1–181.
20. Ismail, W.B.; Mainprice, D. An olivine fabric database: An overview of upper mantle fabrics and seismic anisotropy. *Tectonophysics* **1998**, *296*, 145–157. [CrossRef]
21. Mainprice, D.; Bachmann, F.; Hielscher, R.; Schaeben, H. Descriptive tools for the analysis of texture projects with large datasets using MTEX: Strength, symmetry and components. *Geol. Soc.* **2015**, *409*, 251–271. [CrossRef]
22. Mainprice, D. Seismic anisotropy of the deep Earth from a mineral and rock physics perspective. In *Treatise Geophysics*; Elsevier: London, UK, 2007; Volume 2, pp. 437–491.
23. Bernard, R.E.; Behr, W.M.; Becker, T.W.; Young, D.J. Relationships between olivine CPO and deformation parameters in naturally deformed rocks and implications for mantle seismic anisotropy. *Geochem. Geophys. Geosystems* **2019**, *20*, 3469–3494. [CrossRef]
24. Michibayashi, K.; Ina, T.; Kanagawa, K. The effect of dynamic recrystallization on olivine fabric and seismic anisotropy: Insight from a ductile shear zone, Oman ophiolite. *Earth Planet. Sci. Lett.* **2006**, *244*, 695–708. [CrossRef]
25. Ren, H.; Wang, F.; Xiang, S.; Song, P. Preliminary studies on the microstructure and water content of the Mayoumu harzburgite from the southern Yarlung Zangbo Suture Zone. *Acta Petrol. Sin.* **2016**, *32*, 1653–1662.
26. Mainprice, D.; Barruol, G.; Ismaïl, W.B. The Seismic Anisotropy of the Earth's Mantle: From Single Crystal to Polycrystal. *Am. Geophys. Union* **2000**, *117*, 237–264.
27. Michibayashi, K.; David, M. The Role of Pre-existing Mechanical Anisotropy on Shear Zone Development within Oceanic Mantle Lithosphere: An Example from the Oman Ophiolite. *J. Petrol.* **2004**, *45*, 405–414. [CrossRef]
28. Tommasi, A.; Mameri, L.; Godard, M. Textural and compositional changes in the lithospheric mantle atop the Hawaiian plume: Consequences for seismic properties. *Geochem. Geophys. Geosystems* **2020**, *21*, e2020GC009138. [CrossRef]
29. Chen, C.; Wang, C.Y.; Tan, W.; Yao, Z.-S. Origin of chromite nodules in podiform chromitite from the Kızıldağ ophiolite, southern Turkey. *Ore Geol. Rev.* **2021**, *139*, 104443. [CrossRef]
30. Yudovskaya, M.A.; Costin, G.; Shilovskikh, V.; Chaplygin, I.; McCreesh, M.; Kinnaird, J. Bushveld symplectic and sieve-textured chromite is a result of coupled dissolution-reprecipitation: A comparison with xenocrystic chromite reactions in arc basalt. *Contrib. Mineral. Petrol.* **2019**, *174*, 74. [CrossRef]
31. Boudier, F.; Mainprice, D.; Nicolas, A.; Barou, F. Textural insights into the significance of ophiolitic chromitites, with special reference to Oman. *Tectonophysics* **2021**, *814*, 228972. [CrossRef]
32. Yu, M.; Wang, Q.; Yang, J. Fabrics and water contents of peridotites in the Neotethyan Luobusa ophiolite, southern Tibet: Implications for mantle recycling in supra-subduction zones. *J. Geol. Soc.* **2018**, *176*, 975–991. [CrossRef]
33. Park, M.; Jung, H. Microstructural evolution of the Yugu peridotites in the Gyeonggi Massif, Korea: Implications for olivine fabric transition in mantle shear zones. *Tectonophysics* **2017**, *709*, 55–68. [CrossRef]
34. Soustelle, V.; Tommasi, A.; Demouchy, S.; Ionov, D.A. Deformation and Fluid-Rock Interaction in the Supra-subduction Mantle: Microstructures and Water Contents in Peridotite Xenoliths from the Avacha Volcano, Kamchatka. *J. Petrol.* **2010**, *51*, 363–394. [CrossRef]
35. Cao, Y.; Jung, H.; Song, S.; Park, M.; Jung, S.; Lee, J. Plastic Deformation and Seismic Properties in Fore-arc Mantles: A Petrofabric Analysis of the Yushigou Harzburgites, North Qilian Suture Zone, NW China. *J. Petrol.* **2015**, *56*, 1897–1944. [CrossRef]
36. Higgie, K.; Tommasi, A. Feedbacks between deformation and melt distribution in the crust–mantle transition zone of the Oman ophiolite. *Earth Planet. Sci. Lett.* **2012**, *359–360*, 61–72. [CrossRef]
37. Carter, N.L.; Ave'Lallemant, H.G. High Temperature Flow of Dunite and Peridotite. *Geol. Soc. Am. Bull.* **1970**, *81*, 2181–2202. [CrossRef]
38. Demouchy, S.; Tommasi, A.; Ballaran, T.B.; Cordier, P. Low strength of Earth's uppermost mantle inferred from tri-axial deformation experiments on dry olivine crystals. *Phys. Earth Planet. Inter.* **2013**, *220*, 37–49. [CrossRef]
39. Karato, S.i.; Weidner, D.J. Laboratory Studies of the Rheological Properties of Minerals under Deep-Mantle Conditions. *Elements* **2008**, *4*, 191–196. [CrossRef]
40. Bystricky, M.; Kunze, K.; Burlini, L.; Burg, J.P. High shear strain of olivine aggregates: Rheological and seismic consequences. *Science* **2000**, *290*, 1564–1567. [CrossRef]
41. Jung, H.; Katayama, I.; Jiang, Z.; Hiraga, T.; Karato, S. Effect of water and stress on the lattice-preferred orientation of olivine. *Tectonophysics* **2006**, *421*, 1–22. [CrossRef]

42. Shimada, M.; Kokawa, H.; Wang, Z.; Sato, Y.; Karibe, I. Optimization of grain boundary character distribution for intergranular corrosion resistant 304 stainless steel by twin-induced grain boundary engineering. *Acta Mater.* **2002**, *50*, 2331–2341. [CrossRef]
43. Drury, M.R.; Urai, J.L. Deformation-related recrystallization processes. *Tectonophysics* **1990**, *172*, 235–253. [CrossRef]
44. Halfpenny, A.; Prior, D.J.; Wheeler, J. Analysis of dynamic recrystallization and nucleation in a quartzite mylonite. *Tectonophysics* **2006**, *427*, 3–14. [CrossRef]
45. Passchier, C.W.; Trouw, R.A. *Microtectonics*; Springer Science & Business Media: Berlin, Germany, 2005.
46. Trimby, P.W.; Prior, D.J.; Wheeler, J. Grain boundary hierarchy development in a quartz mylonite. *J. Struct. Geol.* **1998**, *20*, 917–935. [CrossRef]
47. Kruse, R.; Stünitz, H.; Kunze, K. Dynamic recrystallization processes in plagioclase porphyroclasts. *J. Struct. Geol.* **2001**, *23*, 1781–1802. [CrossRef]
48. Prichard, H.M.; Barnes, S.; Godel, B.; Reddy, S.; Vukmanovic, Z.; Halfpenny, A.; Neary, C.; Fisher, P. The structure of and origin of nodular chromite from the Troodos ophiolite, Cyprus, revealed using high-resolution X-ray computed tomography and electron backscatter diffraction. *Lithos* **2015**, *218–219*, 87–98. [CrossRef]
49. Ghosh, B.; Misra, S.; Morishita, T. Plastic deformation and post-deformation annealing in chromite: Mechanisms and implications. *Am. Mineral.* **2017**, *102*, 216–226. [CrossRef]